Correspondence to:
B. Kaifler,
bernd.kaifler@dlr.de

Influences of source conditions on mountain wave penetration into the stratosphere and mesosphere

Bernd Kaifler[1], Natalie Kaifler[1], Benedikt Ehard[1], Andreas Dörnbrack[1], Markus Rapp[1], and David C. Fritts[2]

[1]Institute of Atmospheric Physics, German Aerospace Center, Oberpfaffenhofen, Germany, [2]GATS Inc., Boulder, Colorado, USA

Abstract We present atmospheric gravity wave (GW) measurements obtained by a Rayleigh/Raman lidar at Lauder, New Zealand, (45°S, 170°E) during and after the Deep Propagating Gravity Wave Experiment campaign. GW activity and characteristics are derived from 557 h of high-resolution lidar data recorded between June and November 2014 in an altitude range between 28 and 76 km. In this period, strong GW activity occurred in sporadic intervals lasting a few days. Enhanced stratospheric GW potential energy density is detected during periods with high tropospheric wind speeds perpendicular to New Zealand's Southern Alps. These enhancements are associated with the occurrence of quasi-stationary GW (mountain waves). Surprisingly, the largest response in the mesosphere is observed for conditions with low to moderate lower tropospheric wind speeds (2–12 m/s). On the other hand, large-amplitude mountain waves excited by strong tropospheric forcings often do not reach mesospheric altitudes, either due to wave breaking and dissipation in the stratosphere or refraction away from New Zealand.

1. Introduction

The influence of gravity waves (GWs) on atmospheric dynamics, most notably the residual mesospheric circulation, was first recognized by *Dunkerton* [1978] and *Lindzen* [1981]. GWs play a key role in the vertical coupling of the atmosphere. Excited by various mechanisms mostly at tropospheric levels, GWs propagate through the atmosphere and deposit energy and momentum at the region of dissipation (see, e.g., reviews by *Fritts and Alexander* [2003] and *Plougonven and Zhang* [2014]). To this day, the details and importance of processes regarding the excitation, propagation, and dissipation of GW are not fully understood.

The objective of the Deep Propagating Gravity Wave Experiment (DEEPWAVE) was to "quantify GW dynamics and effects from orographic and other GW sources to regions of dissipation at high altitudes" [*Fritts et al.*, 2015]. The field campaign took place in June/July 2014 on New Zealand's South Island, one of the world's gravity wave hot spots [e.g., *Jiang et al.*, 2003, 2005; *Hoffmann et al.*, 2013]. *Fritts et al.* [2015] provide an overview of initial observations during the campaign as well as definitions of so-called intensive observation periods (IOPs) relating to airborne activities, as well as ground-based IOPs (GBs), to which we will refer in this paper (their Tables 4 and 5). One of the hypotheses of DEEPWAVE was that mountain waves (MW) excited by the flow over the Southern Alps act as a primary source of mesospheric GW activity above New Zealand. Here, ground-based high-resolution lidar observations are analyzed to investigate the vertical propagation of MW into the mesosphere.

2. Instrumentation

The TELMA (Temperature Lidar for Middle Atmosphere Research) instrument developed by the Institute of Atmospheric Physics of the German Aerospace Center is a mobile middle-atmosphere Rayleigh/Raman lidar installed in an 8 ft container. It was set up at the atmospheric research station of the National Institute of Water and Atmospheric Research in Lauder (45.04°S, 169.68°E), New Zealand, in June 2014. TELMA emits 12 W optical power at 532 nm wavelength and 100 Hz pulse repetition rate. Backscattered light is collected using a 63 cm diameter telescope with a field of view of 240 μrad. The fiber-coupled receiver comprises three detector channels, a 608 nm Raman channel and high and low rate 532 nm channels. The detectors are operated in single-photon counting mode and the timing of detected photons is stored with 2 ns resolution. This allows for flexible vertical and temporal binning during data analysis.

3. Data and Analysis

The lidar system was operated at Lauder during and after the DEEPWAVE campaign whenever weather conditions are permitted. In the period between 21 June 2014 and 2 November 2014 the instrument was run on 90 nights totaling 754 h. In this study we use a subset of 557 h which are of good data quality. The longest measurement is 12.3 h and the mean is 7.7 h. Raw photon data from the two 532 nm channels are binned to a 100 m × 2 min grid. The photon count profiles are then smoothed to 900 m × 10 min using a running mean filter. Temperatures are retrieved by integration of the range-corrected photon count profiles assuming hydrostatic equilibrium. In a first step, nightly mean profiles are integrated from top to bottom using seed temperatures from SABER at 100–107 km. Then 2 h averages are formed which are seeded with the nightly mean temperature profile at a lower altitude. In iterating this step with increasing time resolution, temperature profiles with 10 min resolution are finally obtained between 22 and 85 km (typically). Due to increased uncertainties in the retrieved temperatures caused by the presence of aerosols in the lower stratosphere, in this work we limited the GW analysis to altitudes above 28 km.

Temperature perturbations are calculated from the temperature data by removal of estimated time-dependent background profiles. The filter is chosen in a way that both propagating and mountain waves can be isolated from the background. Background temperature profiles are determined from a series of third order polynomial fits of length 20 km which are shifted in altitude by 100 m steps. This method is commonly used for extraction of GW induced perturbations [e.g., *Duck et al.*, 2001; *Alexander et al.*, 2011; *Kaifler et al.*, 2015]. The polynomial fitting method does not involve temporal averaging and is thus able to capture quasi-stationary structures originating from MW which are not retrieved by methods such as the subtraction of nightly means. GW induced perturbations with vertical wavelengths between 2 and 12 km are effectively extracted from retrieved temperature profiles using the polynomial fitting method. We note that this method suppresses waves with vertical wavelengths significantly larger than 12 km, which may cause an underestimate of variance growth with altitude for MW at higher altitudes. Increasing the filter length beyond 12 km leads to mistaking temperature perturbations caused by non-GW sources (e.g., planetary waves, tides, and mesospheric inversion layers) for GW.

Based on extracted temperature perturbations T', the gravity wave potential energy density per mass, E_p, is calculated as a function of altitude z according to

$$E_p(z) = \frac{1}{2} \frac{g^2}{N^2(z)} \overline{\left(\frac{T'(z,t)}{T_0(z,t)} \right)^2}$$ (1)

using the acceleration of gravity g, the Brunt-Vaisälä period N and the background temperature T_0. The overbar denotes a temporal average, here either over the duration of the nightly measurement or 3 h periods. E_p is commonly used to estimate the magnitude of GW activity in a given altitude range [e.g., *Tsuda et al.*, 2000; *Alexander et al.*, 2011]. Due to normalization per mass, its value increases with altitude due to the decrease in air density. In case of conservative wave propagation in a constant background wind field E_p increases exponentially. Comparing measured E_p profiles with calculated profiles assuming conservative propagation of linear GW allows for identification of height regions where wave energy is likely being dissipated.

E_p as calculated from temperature perturbations T' includes contributions from GW originating from orographic sources (MW) as well as other sources. In general, signatures of MW in lidar temperature data appear as quasi-stationary T' patterns, whereas propagating waves are characterized by tilted T' patterns. In order to differentiate between MW and propagating GW, we apply two-dimensional wavelet analysis to the temperature perturbations. The two-dimensional Morlet wavelet [see also *Wang and Lu*, 2010] is ideally suited to discern T' patterns according to their phase angle θ and scale s, the latter corresponding to the wavelength in the direction of propagation. The wavelet parameters θ and s are related to the GW vertical wavelength λ and period τ according to

$$\lambda = \sin^{-1}\theta \left(a_1 s - a_2 \right)$$ (2)

$$\tau = \cos^{-1}\theta \left(b_1 s - b_2 \right),$$ (3)

where the coefficients $a_1, a_2, b_1,$ and b_2 were determined empirically using simulated harmonic waves.
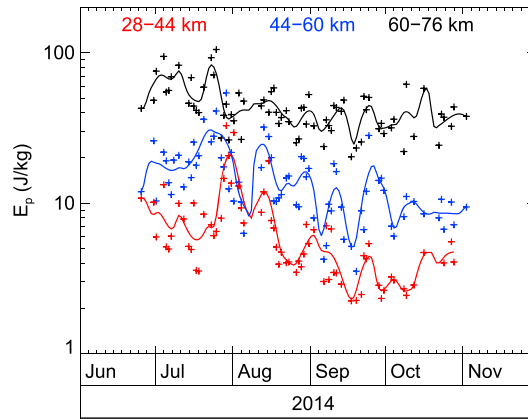
Figure 1. E_p as a measure of GW activity averaged over three different height ranges. Lines represent the time series smoothed with a 10 day Hann window.

Using this method, it is possible to derive E_p for a specific class of GW defined by the phase angle θ which is varied using a step width of 15°. We define three classes: MW ($\theta = 90°$), upward propagating GW ($\theta = 0° \dots 45°$), and downward propagating GW ($\theta = 135° \dots 180°$). The gaps in angle between MW and propagating GW are chosen intentionally in order to clearly differentiate the three classes. We note that the E_p of MW might be slightly underestimated in case of apparent phase propagation due to the changing background wind. Spectral broadening which results from the finite size of the wavelet leads to the variance being distributed over a considerable range in parameter space. By introducing a gap between the three classes, the selectivity is significantly improved.

The procedure to derive E_p for the three classes is as follows: first, for each nightly observation, we compute the wavelet spectrum using the full set of parameters, i.e., one transformation for each pair (θ, s). $T'(z, t)$ can be fully reconstructed from the wavelet spectrum after normalization to the variance of $T'(z, t)$. Next, we reconstruct $T'(z, t)$ only from wavelet transformations with parameters matching the respective class definitions and calculate E_p accordingly. Please note that the relative magnitude of E_p per wave class is depending on the selected range of parameters. As the wavelet transformation also preserves temporal and spatial information, we can derive E_p within intervals of 3 h and in three different height ranges 28–44 km, 44–60 km, and 60–76 km, roughly representing the stratosphere, the stratopause region, and the mesosphere. Thus, we obtain E_p estimates every 3 h for upward propagating, downward propagating, and quasi-stationary waves (MW) at three different height ranges.

4. Results

Mean E_p is shown in Figure 1. As expected, E_p increases with altitude and decreases with time, following roughly the seasonal cycle found in previous studies of GW activity [e.g., *Murayama et al.*, 1994; *Alexander*, 1998; *Kaifler et al.*, 2015]. The temporal evolution of E_p is modulated with a period of 1–3 weeks at nearly all altitudes, and large enhancements are seen in particular at low altitudes.

Strong stratospheric GW activity is detected during the period 29 July to 1 August 2014 (GB21) in conjunction with strong surface winds at Lauder exceeding 20 m/s. However, this event does not lead to significant
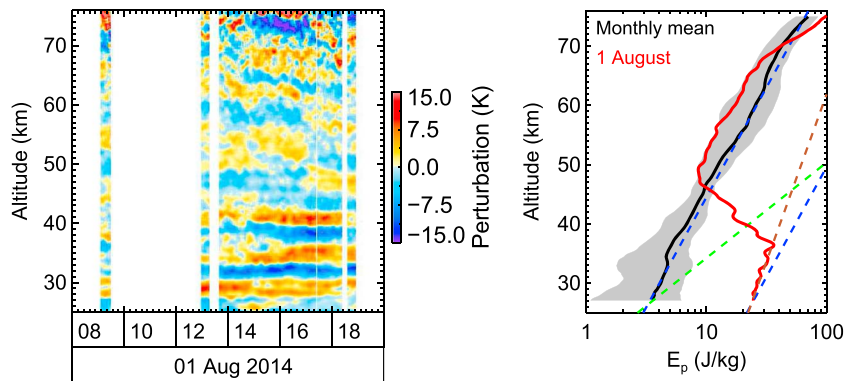

Figure 2. (left) Temperature perturbations and (right) E_p on 1 August (GB21). For reference, the monthly mean for August estimated from observations under quiet MW conditions (10 observations with $|h_{MW}| < 2$ m/s; see discussion for details) is also shown. The shaded area marks the standard error of the mean. Dashed lines mark curves $\exp(z/H)$ (green) assuming conservative propagation, $\exp(z/2.3H)$ (blue) which is from observations and a spectral model that fits mean observations with altitude [*Fritts and VanZandt*, 1993], and $\exp(z/3.5H)$ (brown) as a fit to the observations in the lower stratosphere; $H = 7$ km.
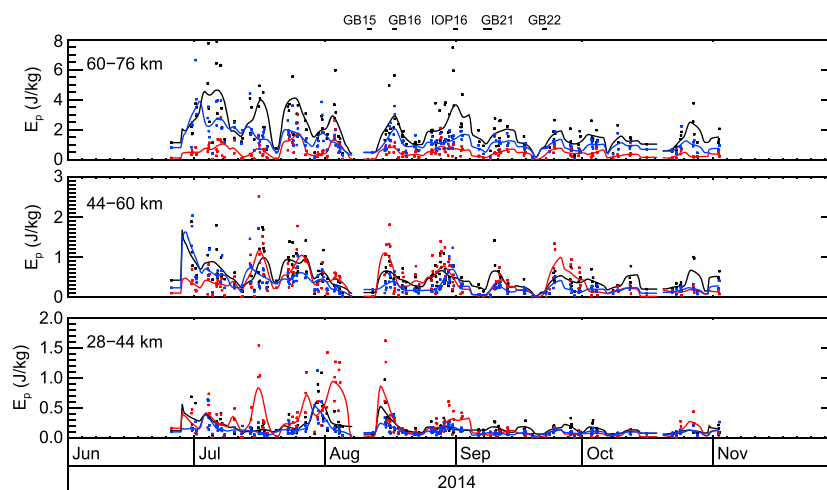
Figure 3. E_p in the height ranges (top) 60–76 km, (middle) 44–60 km, and (bottom) 28–44 km. Colored dots represent 3 h data points based on at least 30 min of observational data. Red: quasi-stationary GW (MW), black: upward propagating GW, and blue: downward propagating GW. Colored lines represent the time series smoothed with a 6 day Hann window.

enhancements in E_p at mesospheric altitudes. Figure 2 shows $T'(z, t)$ and the corresponding E_p profile for 1 August 2014. Quasi-stationary GW with T' up to ± 10 K, $\lambda = 3 \ldots 8$ km and nearly stationary phase are visible for several hours after around 13 UT. MW with comparable amplitudes have been observed previously in the lower stratosphere above northern Scandinavia and Greenland [*Dörnbrack et al.*, 1999; *Doyle et al.*, 2005]. The large-amplitude horizontal structures in Figure 2, which are indicative of MW, cause a dramatic increase in E_p up to ~40 km altitude. On 1 August, the pronounced decrease of E_p between 35 and 45 km altitude is indicative of dissipative processes, e.g., the breaking of the large-amplitude MW. Another possibility is the refraction of MW away from South Island into the polar night jet, caused by changing wind directions with altitude. Although GB21 is the strongest MW event recorded by our instrument, similar signatures of quasi-stationary MW are often observed at Lauder. The much more rapid increase of E_p above 66 km is related to a large mesospheric inversion layer at approximately 75 km (not shown) and downward propagating large-amplitude secondary GW (phase lines progressing upward with time, best visible between 1300 and 1430 UT).

The evolution of E_p per wave class is shown in Figure 3. Generally, E_p of upward propagating waves is larger than E_p of downward propagating waves, and this disparity increases with altitude. In the stratosphere (Figure 3, bottom), large enhancements seen in E_p of quasi-stationary GW (MW) during GB21 and GB22 clearly stand out. While there is still a significant response in the stratopause region for GB22, the MW signal is suppressed in case of GB21. Only weak responses are seen in the mesosphere. The strongest mesospheric MW signal was observed on 25 July (IOP16). Other significant events include 4 July (GB15 and IOP10), 10 July (GB16 and F06), 28 August, 13 September, and 24 September. All of these events are associated with moderate E_p of MW in the stratosphere.

5. Discussion

Stratospheric MW are generated during meteorological conditions of moderate to high tropospheric wind speeds across mountain ranges. Depending on the vertical wind structure and the amplitudes that they achieve at lower altitudes, MW excited near ground level can propagate into the lower stratosphere where they may be subjected to filtering and breaking [e.g., *Eckermann and Preusse*, 1999; *Smith et al.*, 2008]. *Smith et al.* [2009] were the first to observe MW in the mesosphere/lower thermosphere.

There is a well known GW hot spot in the stratosphere above the South Island [e.g., *Jiang et al.*, 2003, 2005; *Hoffmann et al.*, 2013]. Lauder, located 120 km downstream of the Southern Alps (peaks 2500 m), is thus an ideal site for MW observations. In contrast to GW climatologies at polar latitudes [*Yamashita et al.*, 2009; *Alexander et al.*, 2011; *Ehard et al.*, 2014; *Kaifler et al.*, 2015], GW activity at Lauder is dominated by individual events of approximately 1–3 days in duration alternating with quiet intervals resulting in varying conditions for wave generation and vertical propagation (see Figure 1).
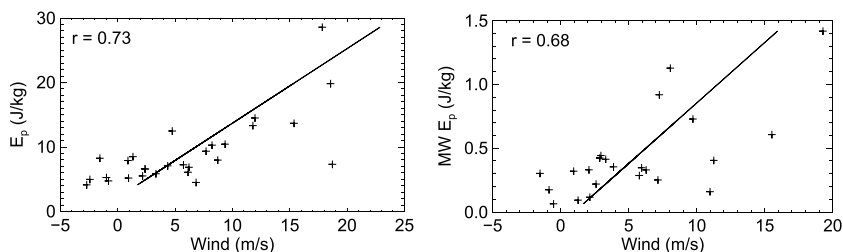
Figure 4. Correlation between (left) wind speed perpendicular to the Southern Alps at 1 km altitude and nightly mean E_p and (right) 3 h averages of MW E_p (based on at least 90 min of observational data) in the stratosphere (28–44 km).

In order to study the relationship between MW forcing and GW activity observed by our lidar at Lauder, we evaluate European Centre for Medium-Range Weather Forecasts (ECMWF) wind fields upstream of the New Zealand South Island (44.2°S, 167.5°E, ~50 km off the coast northwest of Lauder). Using the ECMWF operational model 1 h data sets, the component of the horizontal wind speed perpendicular to the mountain range ($\alpha = 115°$, direction from north-northwest to southeast-east) is averaged over the same intervals during which the lidar acquired data. In line with the analysis of *Yamashita et al.* [2009], we assume that GWs are filtered if the rotation of the horizontal wind vector exceeds 90° in the altitude range 1–30 km. Observations obtained during these conditions are excluded from subsequent analysis. These conditions frequently occur during the months September, October, and November. Figure 4 shows the correlation between ECMWF wind speed upstream of Lauder (and the Southern Alps) at 1 km altitude and GW activity above Lauder for the remaining data sets. Positive values of the correlation coefficient r are found in the lower stratosphere (28–44 km altitude) for total E_p ($r = 0.73$) as well as E_p of MW (red curve in Figure 3, bottom) ($r = 0.68$). The high degree of correlation suggests that a large portion of stratospheric GW activity observed above Lauder is indeed caused by MW, particularly during winter months June, July, and August. When removing the restriction on wind vector rotation, i.e., inclusion of all data sets, the correlation breaks down (correlation coefficients for MW E_p are on the order of 0.1). GW activity in spring appears to be dominated by sources other than MW. Indeed, E_p of stratospheric MW in September and October is significantly less compared to July and August (see Figure 3).

A further potential source for the large-amplitude quasi-stationary GW observed by our lidar is the jet exit region of the tropospheric jet. However, if these waves do propagate into the middle and upper stratosphere, there is no reason as to why this should be possible primarily above the island and to a much lesser degree above the ocean. Satellite observations clearly indicate that there is a GW hot spot above New Zealand, and the strong localization is difficult to bring in line with moving sources such as the jet exit region.

During favorable meteorological conditions for so-called deep propagation, MW can propagate from the troposphere to mesospheric altitudes (e.g., see 25 July in Figure 3). Figure 5a shows that E_p for mesospheric MW reaches a maximum in the range 2–12 m/s (wind at 1 km and wind rotation <90° between 1 and 60 km) and decreases for larger wind speeds. The latter decrease is probably associated with large-amplitude MW breaking in the stratosphere. At high wind speeds MW forcing is so strong that the waves likely become unstable
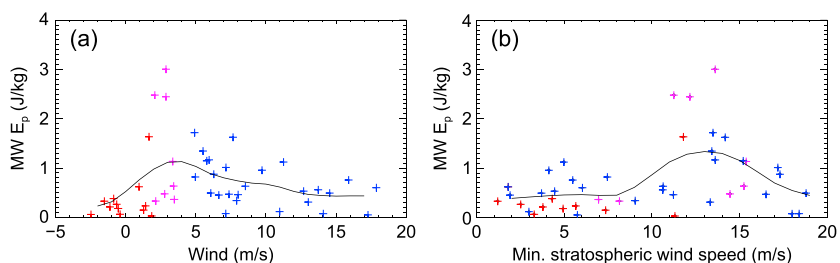

Figure 5. E_p of quasi-stationary GW (MW) from 3 h averages (at least 30 min of observational data) in the height range 60–76 km versus (left) wind speed perpendicular to the Southern Alps at 1 km altitude and (right) minimum wind speed perpendicular to the Southern Alps in the height range 15–40 km. The solid line shows the values smoothed with an 8 m/s Hann window. Colors indicate three different wind speeds (1 km level): <2 m/s (red), 2–4 m/s (magenta), and >4 m/s (blue).

in the lower stratosphere, resulting in an effective reduction of MW activity in the mesosphere. This is consistent with the GV UV lidar observations and WRF modeling shown by *Fritts et al.* [2015], which reveal both dissipation of strong MW in the stratosphere and radiation of secondary GW with nonzero phase speeds at higher altitudes. Changing wind directions with altitude might also cause oblique propagation, refracting the MW away from South Island. In addition to the tropospheric forcing, the minimum stratospheric wind speed is another important factor which controls the vertical propagation of MW. For MW generated under conditions of weak tropospheric forcing (2–4 m/s, magenta symbols in Figure 5) E_p of mesospheric MW shows a large variation. This variation is likely caused by MW encountering critical levels or convective instabilities. In case of weak mean winds, large-amplitude MW can achieve wind amplitudes larger than the mean wind resulting in convective overturning and breaking. Indeed, according to Figure 5b minimum E_p of mesospheric MW is observed when the minimum stratospheric wind speed is below 10 m/s, while maximum E_p occurs for minimum wind speeds above 11 m/s. This implies that moderate forcing conditions (wind speed near ground level in the range 2–12 m/s) and sufficiently high stratospheric wind speeds (>11 m/s) are favorable for MW to reach the mesosphere.

6. Conclusion

We have presented observations of GW activity in the middle atmosphere derived from temperature measurements acquired during winter and spring at Lauder, New Zealand, a midlatitude southern-hemisphere site. The high-cadence observations detected transient GW events which occur periodically in winter (June, July, and August) and significantly enhance the average E_p. Quasi-stationary waves were identified as MW by correlating observed GW activity with the tropospheric wind speed perpendicular to New Zealand's Southern Alps, a proxy for MW forcing. Large-amplitude MW observed during DEEPWAVE did not reach mesospheric altitudes above New Zealand, either due to breaking in the stratosphere or refraction away from South Island. Deep propagation of MW occurs under conditions of weak to moderate forcing and sufficiently stronger stratospheric winds to allow vertical propagation. MW activity peaks in July and August. Later in the season, the rotation of the horizontal wind in the troposphere and lower stratosphere prevents vertical wave propagation. In this case, observed GW activity in the mesosphere is dominated by sources other than MW. A possible candidate are sources in the region of the stratospheric jet. As Lauder is close to the edge of the southern polar vortex, GW generated there may be able to propagate to Lauder.

References

Alexander, M. J. (1998), Interpretations of observed climatological patterns in stratospheric gravity wave variance, *J. Geophys. Res.*, *103*(D8), 8627–8640, doi:10.1029/97JD03325.

Alexander, S. P., A. R. Klekociuk, and D. J. Murphy (2011), Rayleigh lidar observations of gravity wave activity in the winter upper stratosphere and lower mesosphere above Davis, Antarctica (69°S, 78°E), *J. Geophys. Res.*, *116*, D13109, doi:10.1029/2010JD015164.

Dörnbrack, A., M. Leutbecher, R. Kivi, and E. Kyrö (1999), Mountain-wave-induced record low stratospheric temperatures above northern Scandinavia, *Tellus A*, *51*(5), 951–963, doi:10.1034/j.1600-0870.1999.00028.x.

Doyle, J. D., M. A. Shapiro, Q. Jiang, and D. L. Bartels (2005), Large-amplitude mountain wave breaking over Greenland, *J. Atmos. Sci.*, *62*(9), 3106–3126.

Duck, T. J., J. A. Whiteway, and A. I. Carswell (2001), The gravity wave arctic stratospheric vortex interaction, *J. Atmos. Sci.*, *58*, 3581–3596, doi:10.1175/1520-0469(2001)058<3581:TGWASV>2.0.CO;2.

Dunkerton, T. (1978), On the mean meridional mass motions of the stratosphere and mesosphere, *J. Atmos. Sci.*, *35*(12), 2325–2333.

Eckermann, S. D., and P. Preusse (1999), Global measurements of stratospheric mountain waves from space, *Science*, *286*(5444), 1534–1537.

Ehard, B., P. Achtert, and J. Gumbel (2014), Long-term lidar observations of wintertime gravity wave activity over northern Sweden, *Ann. Geophys.*, *32*(11), 1395–1405, doi:10.5194/angeo-32-1395-2014.

Fritts, D. C., and M. J. Alexander (2003), Gravity wave dynamics and effects in the middle atmosphere, *Rev. Geophys.*, *41*(1), 1003, doi:10.1029/2001RG000106.

Fritts, D. C., and T. E. VanZandt (1993), Spectral estimates of gravity wave energy and momentum fluxes. Part I: Energy dissipation, acceleration, and constraints, *J. Atmos. Sci.*, *50*(22), 3685–3694.

Fritts, D. C., et al. (2015), The Deep Propagating Gravity Wave Experiment (DEEPWAVE): An airborne and ground-based exploration of gravity wave propagation and effects from their sources throughout the lower and middle atmosphere, *Bull. Am. Meteorol. Soc.*, doi:10.1175/BAMS-D-14-00269.1, in press.

Hoffmann, L., X. Xue, and M. J. Alexander (2013), A global view of stratospheric gravity wave hotspots located with atmospheric infrared sounder observations, *J. Geophys. Res. Atmos.*, *118*, 416–434, doi:10.1029/2012JD018658.

Jiang, J., S. Eckermann, D. Wu, K. Hocke, B. Wang, J. Ma, and Y. Zhang (2005), Seasonal variation of gravity wave sources from satellite observation, Coupling Processes in the MLT Region, *Adv. Space Res.*, *35*(11), 1925–1932, doi:10.1016/j.asr.2005.01.099.

Jiang, J. H., D. L. Wu, S. D. Eckermann, and J. Ma (2003), Mountain waves in the middle atmosphere: Microwave limb sounder observations and analyses, Middle Atmosphere Structure and Dynamics, *Adv. Space Res.*, *32*(5), 801–806, doi:10.1016/S0273-1177(03)00402-2.

Kaifler, B., F.-J. Lübken, J. Höffner, R. J. Morris, and T. P. Viehl (2015), Lidar observations of gravity wave activity in the middle atmosphere over Davis (69°S, 78°E), Antarctica, *J. Geophys. Res. Atmos.*, *120*, 4506–4521, doi:10.1002/2014JD022879.

Lindzen, R. S. (1981), Turbulence and stress owing to gravity wave and tidal breakdown, *J. Geophys. Res.*, *86*(C10), 9707–9714, doi:10.1029/JC086iC10p09707.

Murayama, Y., T. Tsuda, and S. Fukao (1994), Seasonal variation of gravity wave activity in the lower atmosphere observed with the MU radar, *J. Geophys. Res.*, *99*(D11), 23,057–23,069, doi:10.1029/94JD01717.

Plougonven, R., and F. Zhang (2014), Internal gravity waves from atmospheric jets and fronts, *Rev. Geophys.*, *52*, 33–76, doi:10.1002/2012RG000419.

Smith, R. B., B. K. Woods, J. Jensen, W. A. Cooper, J. D. Doyle, Q. Jiang, and V. Grubisšic (2008), Mountain waves entering the stratosphere, *J. Atmos. Sci.*, *65*(8), 2543–2562.

Smith, S., J. Baumgardner, and M. Mendillo (2009), Evidence of mesospheric gravity-waves generated by orographic forcing in the troposphere, *Geophys. Res. Lett.*, *36*, L08807, doi:10.1029/2008GL036936.

Tsuda, T., M. Nishida, C. Rocken, and R. H. Ware (2000), A global morphology of gravity wave activity in the stratosphere revealed by the GPS occultation data (GPS/MET), *J. Geophys. Res.*, *105*(D6), 7257–7273, doi:10.1029/1999JD901005.

Wang, N., and C. Lu (2010), Two-dimensional continuous wavelet analysis and its application to meteorological data, *J. Atmos. Oceanic Technol.*, *27*(4), 652–666.

Yamashita, C., X. Chu, H.-L. Liu, P. J. Espy, G. J. Nott, and W. Huang (2009), Stratospheric gravity wave characteristics and seasonal variations observed by lidar at the South Pole and Rothera, Antarctica, *J. Geophys. Res.*, *114*, D12101, doi:10.1029/2008JD011472.